Annular variability and eddy-zonal flow interactions in a simplified atmospheric GCM. Part 1: Characterization of high and low frequency behaviour

Article

Published Version

www.reading.ac.uk/centaur

CentAUR

Central Archive at the University of Reading

Reading's research outputs online

Annular Variability and Eddy–Zonal Flow Interactions in a Simplified Atmospheric GCM. Part I: Characterization of High- and Low-Frequency Behavior

SARAH SPARROW

Imperial College London, London, and University of Reading, Berkshire, United Kingdom

MICHAEL BLACKBURN

National Centre for Atmospheric Science, University of Reading, Berkshire, United Kingdom

JOANNA D. HAIGH

Imperial College London, London, United Kingdom

(Manuscript received 17 September 2008, in final form 22 April 2009)

ABSTRACT

Experiments have been performed using a simplified, Newtonian forced, global circulation model to investigate how variability of the tropospheric jet can be characterized by examining the combined fluctuations of the two leading modes of annular variability. Eddy forcing of this variability is analyzed in the phase space of the leading modes using the vertically integrated momentum budget. The nature of the annular variability and eddy forcing depends on the time scale. At low frequencies the zonal flow and baroclinic eddies are in quasi equilibrium and anomalies propagate poleward. The eddies are shown primarily to reinforce the anomalous state and are closely balanced by the linear damping, leaving slow evolution as a residual. At high frequencies the flow is strongly evolving and anomalies are initiated on the poleward side of the tropospheric jet and propagate equatorward. The eddies are shown to drive this evolution strongly: eddy location and amplitude reflect the past baroclinicity, while eddy feedback on the zonal flow may be interpreted in terms of wave breaking associated with baroclinic life cycles in lateral shear.

1. Introduction

Idealized model studies performed by Haigh et al. (2005, hereafter HBD2005) show that stationary forcing in the stratosphere results in latitudinal displacements (shifts) in the midlatitude tropospheric jet. Multiple regression studies of atmospheric analyses (e.g., Haigh 2003; HBD2005; Crooks and Gray 2005) suggest that forcings including solar variability, volcanoes, and the El Niño–Southern Oscillation (ENSO) result in similar shifts of the tropospheric midlatitude jet. Poleward displacement of the jets and storm tracks is also predicted as a response to increased concentrations of greenhouse gases (Yin 2005). Based on idealized model experiments similar to those of HBD2005, Lorenz and DeWeaver

(2007) have interpreted this poleward displacement as a dynamical response to raised tropopause height and increased upper tropospheric baroclinicity associated with predicted warming of the tropical upper troposphere and cooling of the extratropical stratosphere.

The fluctuation–dissipation theorem states that it is possible to generate a linear operator that gives the response of a system to weak external forcing (Ring and Plumb 2007). If the response can be described by a linear operator in this way, it follows that understanding of the atmosphere's natural annular variability may be useful in determining and understanding the jet displacement response to sources of stationary forcing, including those described above.

The influence of the 11-yr solar cycle on upper stratospheric temperatures consists of a small direct radiative effect and an additional indirect effect due to changes in stratospheric ozone (Haigh 1994, 1996). Multiple regression studies of reanalysis data from both the National Centers for Environmental Prediction/National Center

Corresponding author address: Sarah Sparrow, Dept. of Physics, Imperial College London, Prince Consort Road, London, SW7 2BW, United Kingdom.
E-mail: s.sparrow@imperial.ac.uk

for Atmospheric Research (NCEP/NCAR) and the European Centre for Medium-Range Weather Forecasts [40-yr Re-Analysis (ERA-40)] have shown signals in wind and temperature due to the solar cycle extending into the troposphere (Haigh 2003; HBD2005; Crooks and Gray 2005). The possible influence of the solar cycle on the tropospheric flow is not well understood, although it is thought to manifest itself via stratosphere–troposphere interactions as opposed to a direct effect (e.g., Bates 1981; Haigh 1996, 2003; Kuroda and Kodera 2005; Salby and Callaghan 2006; Kodera and Shibata 2006; Kuroda et al. 2007).

Aside from solar cycle influences, the impact of the stratosphere on tropospheric flow regimes has been an area of much recent interest (e.g., Baldwin and Dunkerton 1999, 2001; HBD2005; Haynes 2005; Kushner and Polvani 2004; Charlton et al. 2004; Wittman et al. 2004; Song and Robinson 2004; Kodera 2006). In HBD2005, changes in the stratospheric equilibrium temperature distribution in an idealized model lead to changes in the strength and position of the tropospheric jet and of the mean meridional circulation, including the extent of the Hadley cells. This study has been extended by Simpson et al. (2009) to show that changes in wave refraction initiated by changes in the potential vorticity gradient associated with altered temperature gradients and wind shears at the tropopause are important in driving the tropospheric circulation changes. Simpson et al. also show that the location and latitudinal extent of these tropopause changes are important in determining the direction of displacement of the tropospheric jet.

So far we have discussed studies that examine the effects of forcings such as the solar cycle or other stratospheric processes on the tropospheric jet. However, the tropospheric jet itself exhibits natural variability and, if fluctuation–dissipation theory holds, understanding tropospheric flow regimes may be important for determining the response to such forcings. Numerous previous studies have examined zonal-mean tropospheric flow regimes in both models and observations (e.g., James and James 1992; James et al. 1994; James and Dodd 1996; Lorenz and Hartmann 2001, 2003; Son and Lee 2006; Lee et al. 2007; Gerber and Vallis 2007; Vallis and Gerber 2007). James et al. demonstrate that, for a simple global circulation model, wave–mean flow interactions give rise to an intrinsic long time scale and may be implicit in the generation of low-frequency variability with time scales greater than a year. The more recent model study of Gerber and Vallis (2007) also suggests that interactions between synoptic eddies and the large-scale flow establish a separate intraseasonal time scale, which is shown to be independent from the main internal model time scales. Model studies of migrating zonal jet regimes have

also been conducted in the ocean by Chan et al. (2007). They propose a mechanism to explain the equatorward migration of secondary meridional jets. They show that the eddy heat fluxes have a poleward bias that leads to the jets' equatorward migration. Chan et al. speculate that the asymmetry in the eddy heat fluxes is consistent with larger Eady growth rates associated with smaller values of static stability on the poleward side of the jets.

In this study we consider changes in the tropospheric jets by utilizing a phase space approach to examine the combined fluctuations of the two leading modes of variability of the zonal mean flow [as introduced by James et al. (1994)] in the Newtonian forced model of HBD2005. By understanding the processes involved in controlling the natural variability of the tropospheric flow in this way, it is hoped that further insight may be gained into how forcings to the system result in the observed changes seen in HBD2005. The response on different time scales is examined and eddy–mean flow interactions considered.

This is a multiple part study in which this paper (Part I) will characterize the behavior of the tropospheric jets in our model at high and low frequencies and consider eddy–mean flow forcing and feedbacks. In Part II a detailed examination of the mechanisms resulting in high and low-frequency jet behavior will be presented. The phase relationship between the wave source and current wind distribution will be shown to be important in determining the latitudinal direction of jet migration. Part III will look at the impact of external forcings on the jet variability. The same mechanism and behavior will be shown to operate in all situations with the difference in simulations corresponding to a shift in time scales of the high- and low-frequency behavior.

This paper is structured as follows: In section 2, a brief description of the model and experimental configuration is given; section 3 presents the results. This is divided into several subsections, the first of which looks at the leading modes of variability as defined by empirical orthogonal functions and how they relate to the time-mean structure of the tropospheric jet. A frequency analysis of the modes of jet variation and eddy forcing follows. In section 3c, phase space trajectories are studied at both high and low frequencies. To characterize phase space evolutions the vertically integrated zonal momentum budget is examined. The final part of the results section looks at Eliassen–Palm fluxes and mean flow feedbacks. The conclusions are given in section 4.

2. Model

A simplified global circulation model (sGCM), the same model as in HBD2005, is used to study zonal flow
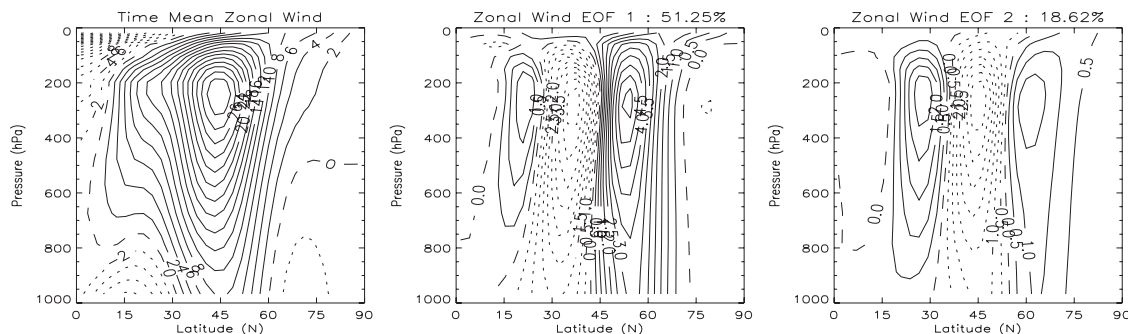
FIG. 1. (left) Latitude–height section of time mean $[u]$ and the corresponding (middle) EOF 1 and (right) EOF 2 of $[u]$. Contour interval is 2 m s^{-1} for the mean jet and 0.5 m s^{-1} for the EOF patterns. The percentage variance explained by each EOF is given in the figure title.

regimes in the troposphere. The model uses the spectral dynamical core described previously by Hoskins and Simmons (1975), modified to include the angular-momentum-conserving vertical discretization of Simmons and Burridge (1981) but retaining the original sigma coordinate. The simulation uses T42L15 resolution, denoting triangular isotropic spectral truncation at a total wavenumber 42, equivalent to an equatorial grid spacing close to 475 km for the equivalent linear transform grid, and 15 levels between the surface and about 18.5 hPa. The model levels are chosen to increase resolution around the tropopause (the model levels are at 18.5, 59.5, 106, 152, 197, 241, 287, 338, 400, 477, 569, 674, 784, 887, and 967 in units of 1000σ).

The model climate is maintained using the linear forcing and drag scheme of Held and Suarez (1994) in place of the moist parameterizations of a sophisticated GCM. Orography is omitted. The temperature is relaxed toward a zonally symmetric equilibrium distribution (HBD2005, their Fig. 2a) on a time scale that is 40 days above the boundary layer ($1000\sigma > 700$ hPa) but is reduced to 4 days at the equatorial surface. Rayleigh friction is also included in the boundary layer with a time scale of 1 day at the surface. The simulation was run for 10 200 days, the initial 200 of which were discarded for spinup.

3. Results

The model climate is described by HBD2005. The dynamical response to the applied temperature relaxation results in the formation of a positive latitudinal temperature gradient above the tropopause and a temperature gradient in the troposphere that is less negative than that of the applied T_e (see Fig. 2b of HBD2005). The modeled zonal wind field, in thermal wind balance with the temperature distribution, consists of a tropospheric westerly jet centered at 45° latitude in each hemisphere, shown in Fig. 1.

a. Leading modes of variability

The dominant modes of annular variability within the model simulation were calculated using principal component (PC) analysis from a daily time series of zonal-mean zonal wind. Data from both hemispheres were treated as independent samples (see HBD2005), giving 20 000 days of hemispheric data from the 10 000-day simulation and fields were weighted both horizontally and vertically to give their mass-weighted contribution to the variance (following Baldwin et al. 2009). Figure 1 shows the time-mean zonal-mean zonal wind (on the left) and the first two empirical orthogonal functions of zonal-mean zonal wind, which together explain around 70% of the variance (51.25% from EOF1 and 18.62% from EOF2). The EOF patterns are presented in meters per second by projecting the anomaly data onto the normalized principal component time series. The middle panel in Fig. 1 shows EOF1, which is a deep structure throughout the troposphere and represents north–south displacement of the midlatitude jet relative to its mean position at around 45°N (cf. the left panel). The EOF2 pattern (Fig. 1, right) is similarly deep and represents both broadening/narrowing and weakening/strengthening of the midlatitude jet. Note that there is a marked vertical tilt poleward with height on the equatorward side of the jet, particularly in EOF1. The HBD2005 responses to idealized stratospheric forcings project strongly onto these two leading EOFs (not shown), suggesting that they describe a large part of the total observed response. This strengthens the premise that study of these two modes of variability may yield important insights into how the HBD2005 responses are produced.

b. Frequency analysis

Lorenz and Hartmann (2001, hereafter LH2001) show that, in the Southern Hemisphere, high-frequency
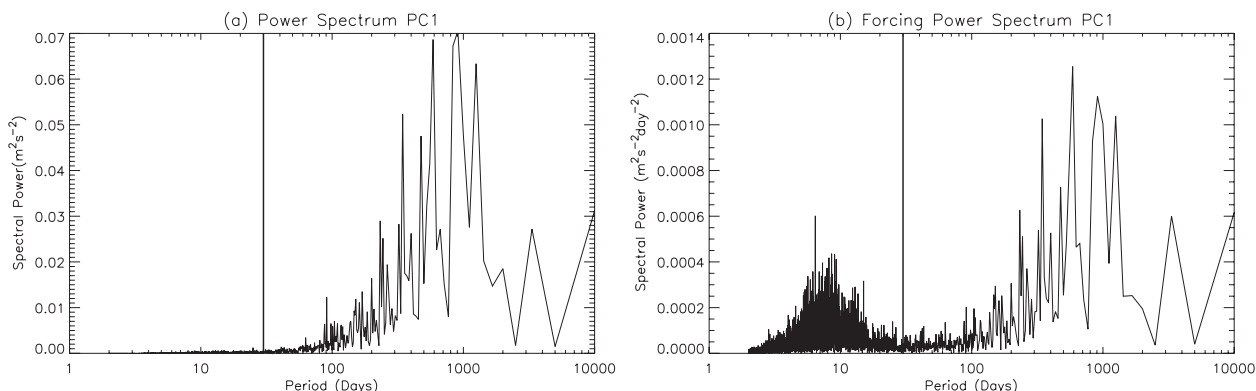
FIG. 2. Power spectra of PC1 for (a) zonal-mean zonal wind and (b) horizontal eddy momentum forcing. The vertical line corresponds to a 30-day period.

synoptic eddies feed back positively on the zonal mean wind anomalies and that this feedback is important for the selection of the leading pattern of variability. They also show that the zonal wind power spectrum extends over much lower frequencies than the eddy forcing power spectrum, leading to a difference in the characteristic time scale between the zonal wind and eddy forcing (see Fig. 4 in LH2001). In this study we are primarily interested in the response to stationary forcing and therefore are interested in the slowest modes of variability (represented by EOF1 and EOF2).

Following the analysis by LH2001 and Lorenz and Hartmann (2003), the zonally averaged zonal momentum equation can be expressed as

$$\frac{\partial [u]}{\partial t} = -\frac{1}{a \cos^2 \phi} \frac{\partial}{\partial \phi} ([u'v'] \cos^2 \phi)$$
$$-\frac{1}{a \cos^2 \phi} \frac{\partial}{\partial \phi} ([u][v] \cos^2 \phi)$$
$$-\frac{\partial}{\partial p} [u\omega] + f[v] + [F_\lambda], \quad (1)$$

where square brackets denote zonal average, a prime denotes the departure from the zonal average, u is the zonal wind, v is the meridional wind, ω is the vertical wind, ϕ is latitude, t is time, a is the earth's radius, and F_λ is the zonal frictional force. The first term on the rhs of Eq. (1) will be referred to as the eddy momentum forcing. This is the term that will be used later in the vertical integral and, so, is the focus here. The Coriolis term, $f[v]$, is important locally but, owing to mass continuity, is almost zero in the vertical integral.

Figure 2 shows (left) power spectra for $[u]$ projected onto EOF1 and (right) the eddy momentum forcing

term projected onto EOF1. The eddy momentum forcing spectrum projected onto the PC1 time series has two distinct peaks at high and low frequencies corresponding to periods of around 8 days and several hundred days, respectively. The low-frequency (long period) component exhibits a redness that is present in both the eddy forcing and $[u]$ spectra. The high-frequency (short period) portion of the $[u]$ spectrum is negligible compared to the low-frequency signal in the $[u]$ spectrum. The corresponding spectra for PC2 are shown in Fig. 3. The low-frequency component is much reduced in PC2 for both spectra, showing that there is increased power at longer time scales in PC1 compared to PC2. The high-frequency component in the forcing term of PC2 remains. This is consistent with the observational results of LH2001, but the separation between the high- and low-frequency components can be seen more clearly here by using a logarithmic scale for the period. Note that the eddy momentum forcing spectra show the total eddy momentum forcing in Eq. (1) at high and low frequencies (i.e., the total effect due to eddy fluctuations at all frequencies). Throughout the rest of this paper the definition of high and low frequencies is determined by the apparent break point near the 30-day period, indicated by the vertical line in Figs. 2 and 3. The results are relatively insensitive to the exact period used to distinguish high and low frequencies.[1] For PC1 the split of $[u]$ variability at high/low frequencies is 13%/87% (consistent with the spectra in Fig. 2). As expected from Fig. 3, the relative contribution of PC2 at lower frequencies is reduced and the high/low-frequency ratio is 40/60. For the eddy momentum forcing spectra the corresponding high/low-frequency ratios are 87/13 and 95/5

---

[1] These spectra are similar for models with different numbers of vertical levels.
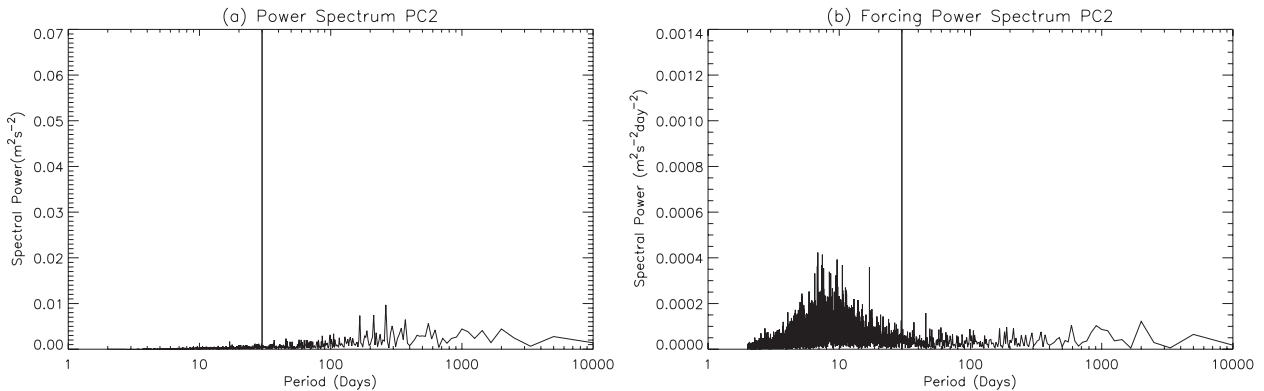
FIG. 3. As in Fig. 2 but for PC2.

for PC1 and PC2, respectively. This shows that the forcing is dominated by high-frequency variability and, as with [*u*], the low-frequency contribution is reduced for PC2.

c. Phase space trajectories

A phase space view of the variability can be constructed by plotting PC1 amplitude against PC2 amplitude for each point in the simulation. Figure 4 shows contours of a 2D probability density function (PDF) constructed from the phase space locations of the zonal-mean zonal wind in the simulation. For each bin in the PDF a mean trajectory can be calculated (represented by the arrows in the diagram) that indicates where on average a point in the bin is moving next in phase space. These plots are similar in construction to the phase space pictures of James et al. (1994). Unfiltered data in

Fig. 4a show no coherent movement in phase space where the points are densest near the origin, with mean trajectory arrows pointing in apparently random directions. The trajectory appears clockwise toward the edge of the distribution (i.e., large PC1/PC2 amplitude): this will be discussed further later in this section.

However, when a 30-day Lanczos low-pass filter (as used in LH2001) is applied to the PC time series (Fig. 4b), there is a distinct anticlockwise circulation, even where the points are densest. The circulation time scale, τ_c, calculated as the time between subsequent passes of the same phase angle, has a wide range of values, consistent with the redness seen in the spectra (Figs. 2 and 3). It is therefore misleading to quote a single circulation time for this picture, but, as an indication, the mean circulation time scale is 82 days with a standard deviation of 27 days. The distribution of points in phase space is elongated along the PC1 axis, which indicates that

FIG. 4. Probability density function of zonal-mean zonal wind in PC1/PC2 phase space (contours) and average trajectory for each bin in the PDF (arrows) for (a) unfiltered, (b) 30-day Lanczos low-pass filtered, and (c) 30-day Lanczos high-pass filtered data. Bin size is 0.3 × 0.3 m s^{-1}. The contours are logarithmically spaced and represent the percentage of time spent in unit area of phase space. In (b) the arrow length has been multiplied by 2 and in (a) and (c) by 0.5.

most of the low-frequency variability is contained in this mode.

Applying a 30-day Lanczos high-pass filter to the data (Fig. 4c) reveals a clockwise circulation in phase space. The high-frequency component has less spread in circulation time scale than is displayed at low frequencies, so it is possible to quote a single value for τ_c of ~8 days. The distribution of points in phase space is more circular than at low frequencies, indicating that PC1 and PC2 contribute approximately equally to the high-frequency variability. These results are consistent with the spectra shown in Figs. 2 and 3.

The clockwise rotation noted earlier at large PC1/PC2 amplitudes for the unfiltered data may be explained as follows: The peak PC1/PC2 amplitudes in Fig. 4 are larger for the unfiltered time series than for the low-frequency time series, suggesting that the peak unfiltered amplitudes can only be reached by high-frequency epicycles adding to the low-frequency amplitude. Therefore, the unfiltered distribution at high amplitude reflects the high-frequency clockwise trajectory.

Figure 5 shows example phase space trajectories from two periods of the model integration during which there is poleward migration of the Northern Hemisphere jet. The two periods are highlighted in a 1000-day time series of zonal-mean zonal wind anomalies at 240 hPa (Fig. 5, top). Phase space trajectories for periods 1 and 2 are shown in the middle and bottom rows, respectively, with time increasing from blue to red. Trajectories of the unfiltered and 30-day low-pass filtered data are shown for the whole period. Trajectories of the 30-day high-pass filtered data are shown for a representative 30-day section from the middle of each chosen period for clarity. Period 1 lasts 150 days during which a complete revolution of phase space is completed. The unfiltered trajectory shows broadly the low-frequency anticlockwise circulation with high-frequency variability superimposed, including several distinct clockwise epicycles of varying amplitude. A large amplitude epicycle is visible (in green) at low values of PC2, while smaller amplitude epicycles occur in the blue and yellow portions of the trajectory. The low-frequency trajectory shows a smooth, almost elliptical anticlockwise evolution, with small deviations in the blue and yellow portions. The high-frequency trajectory from this period shows the expected clockwise evolution as indicated by Fig. 4. Period 2 lasts longer (250 days) and similarly shows anticlockwise (clockwise) phase space circulation at low (high) frequencies. In contrast to period 1, the low-frequency evolution passes through the peak of the phase space density and is more disturbed. Contrasting the low-frequency behavior in the two periods illustrates the range of trajectories and time scales that exists in the simulation. This

range of behavior is summarized for the whole simulation in Fig. 4. In contrast, the high-frequency behavior during the two periods is qualitatively similar.

To further confirm the phase space rotations at all frequencies, the analysis by Chan et al. (2007) is followed. Eight 45° sectors of phase space were defined with boundaries centered about the axes, and the percentage of times a given sector was preceded by each of the remaining seven sectors calculated. To summarize these results, the unfiltered time series shows that sectors are preceded 45.7% of the time by the adjacent clockwise sector and 40.4% of the time by the adjacent anticlockwise sector. The other sectors make up the remaining 13.9%. This reflects the lack of coherent phase space rotation noted in Fig. 4a. Indeed, Fig. 5 and animations of phase space trajectories, although noisy, show high-frequency clockwise epicycles superimposed on a low-frequency anticlockwise rotation. By compositing high-frequency data based on a low-frequency sector (not shown), it is deduced that the amplitude and nature of the high-frequency circulation is independent of the low-frequency sector. At low frequencies, sectors are preceded 34.3% of the time by the adjacent clockwise sector and 63.2% of the time by the adjacent anticlockwise sector, with the other sectors making up the remaining 2.5%. This shows that the anticlockwise evolution, noted in Fig. 4b, is followed most of the time. At high frequencies, sectors are preceded 45.0% of the time by the adjacent clockwise sector and 24.4% of the time by the adjacent anticlockwise sector. The contribution from the other sectors of 30.6% is larger than in the unfiltered and low-frequency time series, although the next largest contribution in this group is 12.4%. This reflects the poorer temporal resolution of the high-frequency data compared to the circulation time scale; however, the clockwise evolution is still reflected by the largest percentage. Phase space trajectories for other model simulations exhibit the same behavior at high and low frequencies and are included in the appendix.

To establish what happens to the midlatitude jet as a phase space circulation is completed, composite averages of zonal-mean zonal wind were taken for all points lying within 45° sectors of phase space. Figure 6 shows composite average pictures for [u] based on the low-pass filtered PC1/PC2 time series. Note the sector boundaries are centered about the axes and sectors are labeled with +, −, or 0 to indicate high, low, or neutral PC1 and PC2 values, respectively. For example, sector +0 indicates high PC1 values and neutral PC2 values and represents points within the ±22.5° range in phase space. Starting at sector −+ and moving anticlockwise around the panels, the midlatitude jet is seen to shift poleward through to sector ++. Over the same evolution the winds strengthen

FIG. 5. (top) Time series of zonal-mean zonal wind anomalies at 240 hPa for a 1000-day section of the simulation. Red and blue colors indicate positive and negative wind anomalies, respectively. Phase space trajectories (from blue to red) (middle row) for period 1 and (bottom row) period 2 of (left) unfiltered, (middle) 30-day low-pass filtered, and (right) 30-day high-pass filtered data. The high-pass filtered trajectories show only 30 days from the middle of each chosen period with altered axes. Contours represent the PDF distributions for the entire simulation, as in Fig. 4.

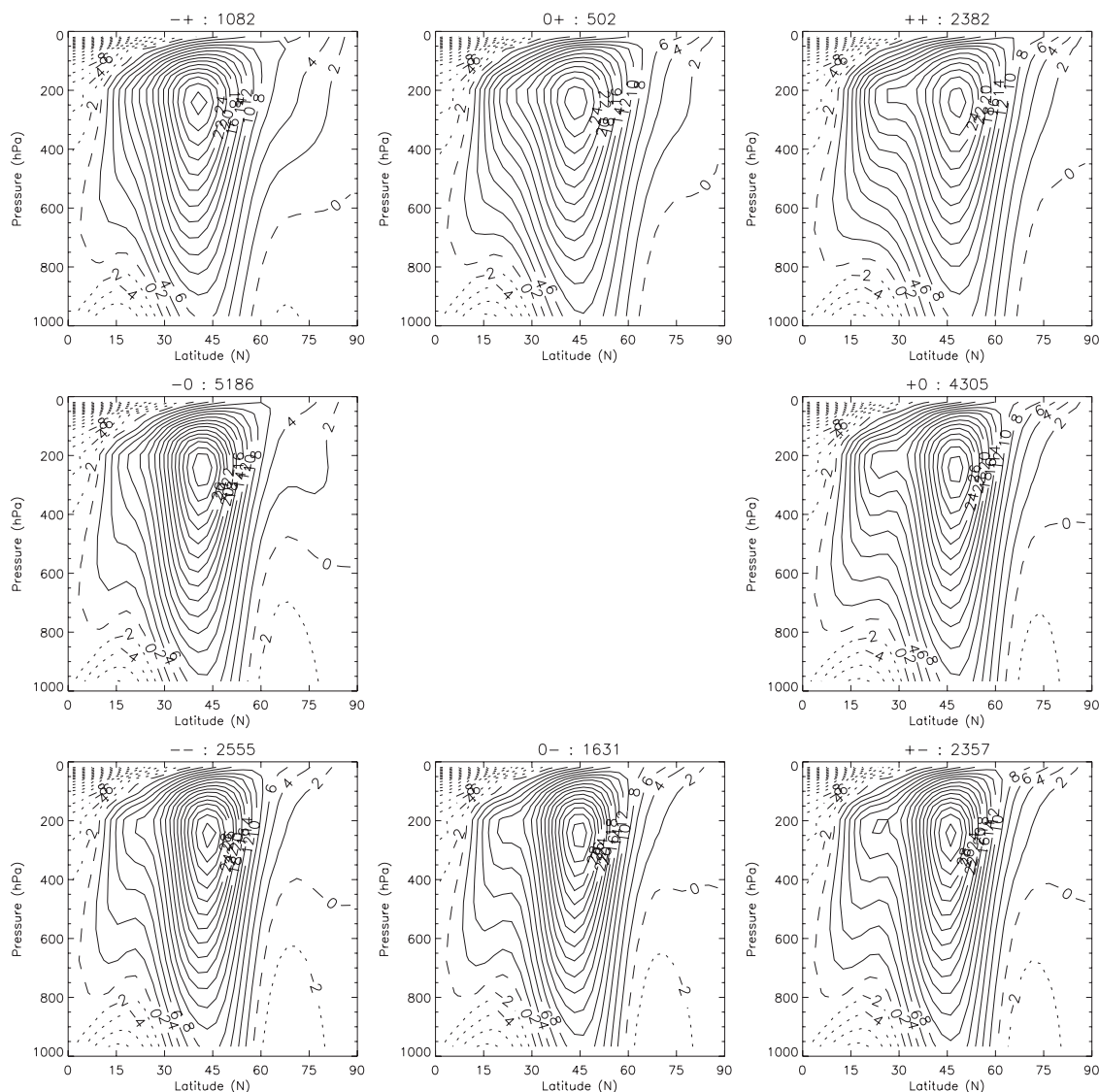FIG. 6. Thirty-day Lanczos low-pass filtered sector composites of zonal-mean zonal wind. The title of each plot indicates the sign of PC1 and PC2, respectively, and the number of points in each composite picture. The contour interval is 2 m s^{-1}.

in the subtropics, giving rise to the "double-jet" structure seen in these sectors. During the evolution from sector $++$ through to sector $-+$, the poleward portion of the jet at $\sim 50°$N in sector $++$ is no longer sustained so far poleward and collapses, decreasing in amplitude and merging with the new growing subtropical jet. This process has been verified by studying a series of 4° sector composite averages through this region of phase space (not shown). The behavior of this evolution is qualitatively similar to the "Rossby wobblers" noted by James and Dodd (1996) or, more recently, the poleward propagation regime of Lee et al. (2007).

There is a substantial reduction in the number of points contributing to the 0+ sector compared to other

sectors at low frequencies (Fig. 4b). This could reflect a more rapid trajectory for positive PC2 and neutral PC1, leading to fewer days in the sector, and/or avoidance of this sector by the trajectory. There is evidence for both effects. On the one hand, the mean trajectory vectors in Fig. 4b do suggest a rapid transit of sector 0+ (but no more than for sector $+-$). An example is seen in the low-frequency trajectory for period 1 in Fig. 5, where the greatest separation of points occurs in sector 0+. On the other hand, the sector transition statistics discussed previously show that the anticlockwise evolution occurs less frequently in sector 0+ than during the poleward migration phase. An example of avoidance of sector 0+ is seen in the low-frequency trajectory for period 2 in
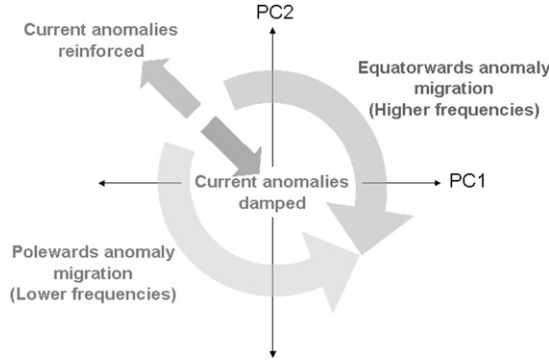
FIG. 7. Schematic diagram highlighting the effect of radial and tangential movements in phase space.

Fig. 5. A broad, weak jet at 45° therefore occurs relatively infrequently: indeed, the entire low-frequency distribution is displaced toward negative PC2, suggesting that a stronger, narrower jet than the climatological average is favored during poleward propagation.

d. Vertically integrated zonal momentum budget

Having established that the time evolution of the flow described by the first two tropospheric modes of variability can be represented as a clockwise (anticlockwise) trajectory in phase space at high (low) frequencies (as summarized in Fig. 7), it is possible to examine the driving mechanism of these trajectories by considering sector composite averages of the vertically integrated zonal momentum budget.[2] Following appendix B of HBD2005, the vertically integrated zonal momentum budget can be expressed as

$$\frac{1}{g}\frac{\partial}{\partial t}\int_0^{p_s}[u]\,dp = -\frac{1}{1/ga\cos^2\phi}\frac{\partial}{\partial\phi}\cos^2\phi$$
$$\times \int_0^{p_s}([u][v]+[u'v'])\,dp + \frac{1}{g}\int_0^{p_s}[F_\lambda]\,dp$$
$$= C_{\mathrm{ZONAL}} + C_{\mathrm{EDDY}} + [\tau_{S\lambda}], \qquad (2)$$

where $[\tau_{S\lambda}]$ is the zonally averaged zonal component of the surface stress, g is the acceleration due to gravity, C_{EDDY} is the vertically integrated horizontal eddy momentum flux convergence in Eq. (1), and C_{ZONAL} is the horizontal momentum flux convergence due to the zonal mean flow.

Figure 8 shows the low-frequency sector composite averages of the vertically integrated zonal momentum budget. With the exception of sector 0+, the zonal wind

---

[2] Time filtering is applied only to the PC time series and not to the individual components of the vertically integrated momentum budget.

tendency [lhs of Eq. (2)] can be described as mainly a balance between C_{EDDY} and $[\tau_{S\lambda}]$. In a manner consistent with the zonal wind progression, the dipole pattern dominating the eddy momentum forcing and stress terms progresses poleward for anticlockwise motion between sectors −+ and ++. There is a slight mismatch in the latitude of peak $[\tau_{S\lambda}]$ and peak C_{EDDY}, particularly at low latitudes, due to the vertical tilt of the zonal wind anomalies with height on the equatorward side of the jet (see Fig. 1; the vertical integral of the zonal wind will be located farther poleward than the surface stress, which is aligned with the bottom of the jet).

The corresponding high-frequency sector composites of the vertically integrated zonal momentum budget are shown in Fig. 9. In this case the zonal wind tendency is larger and follows the eddy term more closely. The surface stress contributes less to the high-frequency circulation, as its impact on the vertically integrated flow is on a time scale comparable to or longer than that of the high-frequency circulation itself. Note that, since the circulation is clockwise in phase space, the evolution between panels should also be consistent. Anomalies grow on the poleward side of the jet and move equatorward for a clockwise movement between sectors 0+ and −+. In sector −+ the equatorward anomaly is dying out and a new anomaly is growing on the poleward side of the jet. At high frequencies there is a smooth transition between this growth and decay phase of anomalies, so the trajectory is represented by a more circular distribution in phase space (as seen in Fig. 4c).

The high- and low-frequency vertically integrated momentum budgets can be usefully summarized by projecting the budget terms onto the 1D EOF patterns and representing them as tendency vectors in phase space (Fig. 10). The x and y components for a tendency vector are given by the projection coefficients of that term onto EOF1 and EOF2, respectively. The tails of the vectors are centered on the composite mean position. Note that the 1D EOF patterns (not shown) are calculated from vertically integrated $[u]$ and have spatial correlations of 0.9998 (EOF1) and 0.9980 (EOF2) with the vertical integrals of the 2D EOF patterns shown in Fig. 1. Radial components of the vectors in Fig. 10 correspond to forcing or damping of the state represented by that point in phase space, and tangential components of the vectors drive the evolution around phase space (as illustrated by the schematic diagram in Fig. 7).

Figure 10a shows such vectors plotted for the low-frequency composite mean trajectory. It is evident that there is an approximate balance between the eddy and surface stress terms, which is indicative of a quasi-equilibrium situation. However, the surface stress points in advance of the origin in phase space; that is, it has a
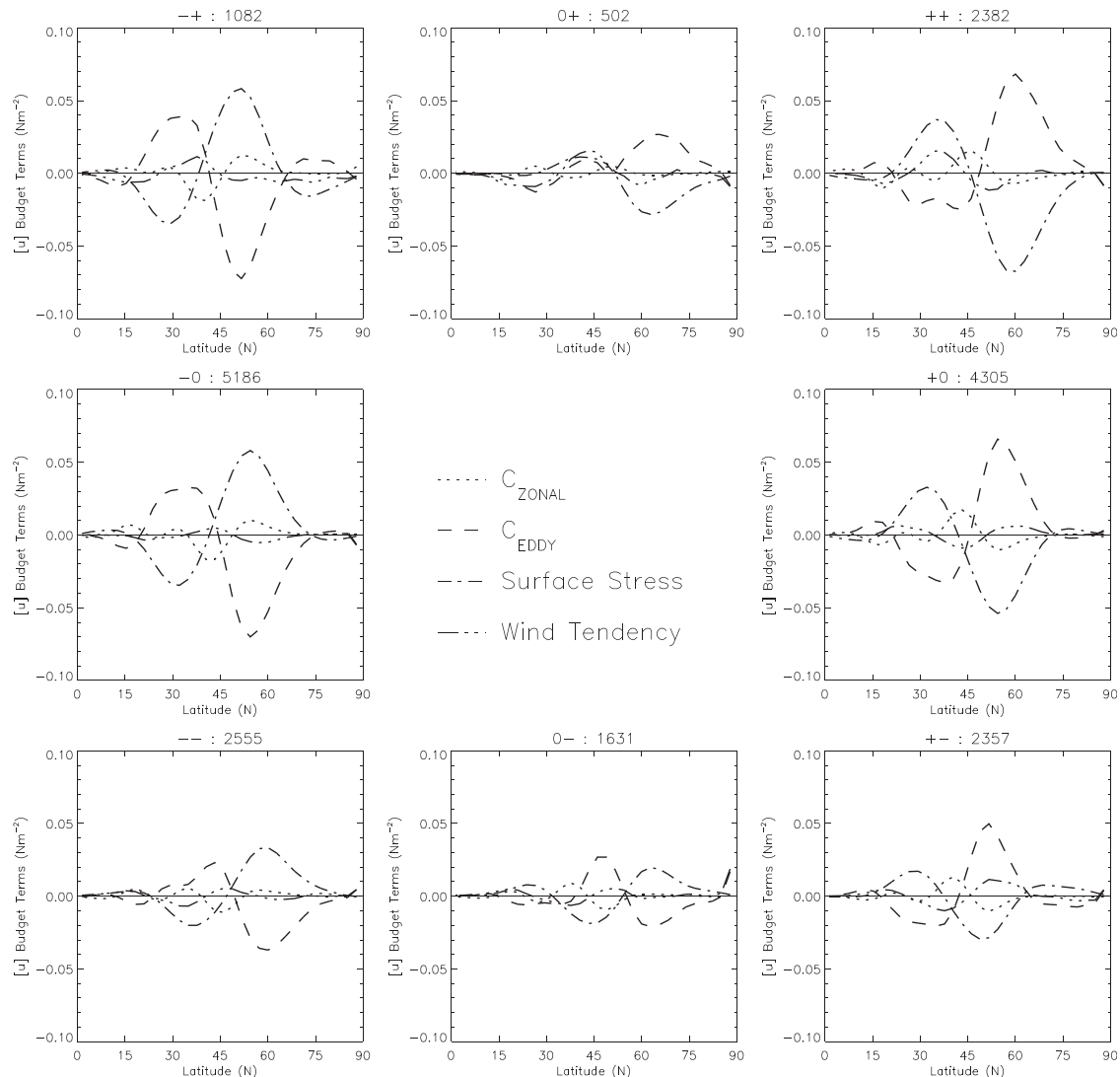
FIG. 8. Thirty-day Lanczos low-pass filtered sector composites of the vertically integrated momentum budget anomalies: Convergence of the flux of westerly momentum resulting from the zonally asymmetric eddies, C_{EDDY}, (dashed line); the zonally averaged flow, C_{ZONAL} (dotted line); the surface stress, $[\tau_{S\lambda}]$ (dashed–dotted line); and the resultant wind tendency (dashed–triple dotted line). The sign of PC1/PC2 and number of points in each composite picture are given in the panel titles.

significant tangential component that at first sight appears to be driving the phase space circulation. Taking an instantaneous view, this tangential component can be explained by the mismatch in latitude of the surface stress and wind anomalies due to vertical tilt of wind anomalies on the equatorial side of the jet. Alternatively, from a time evolving perspective, the direction of the surface stress could equally be explained as a lagged response to the eddy perturbations that are driving the circulation. This can be established from phase angle lagged correlations between C_{EDDY} and $[\tau_{S\lambda}]$ (not shown).

At high frequencies (Fig. 10b) it is clear that the phase space circulation is strongly driven by the eddy momen-

tum forcing and there is less contribution by the surface stress to the circulation. It is the eddy term that most dramatically changes between the high and low frequencies, whereas the stress term exhibits less change because it is linear.

e. Eliassen–Palm fluxes and mean flow feedbacks

Having characterized the vertically integrated eddy forcing of the zonal mean flow at high and low frequencies, the distribution of eddy forcing and the associated eddy fluxes and structures are now examined in the meridional plane. Using the transformed Eulerian mean framework, the Eliassen–Palm (EP) flux facilitates
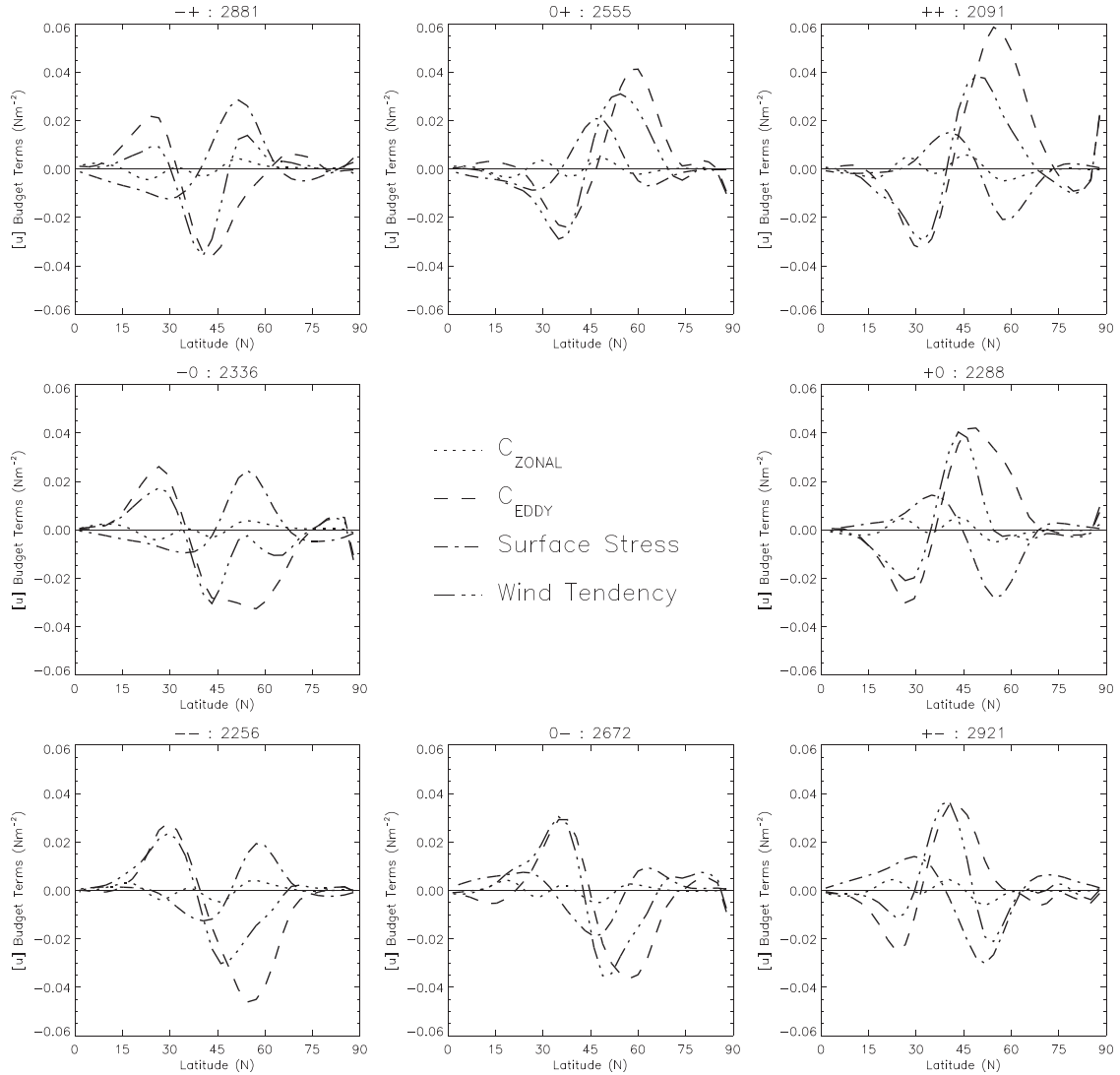
FIG. 9. As Fig. 8 but using 30-day Lanczos high-pass filtered data. Note also the change in scale on the *y* axis.

diagnosis and interpretation of both eddy momentum and heat fluxes and the net eddy forcing of the mean flow (Edmon et al. 1980). From Andrews et al. (1987), the EP flux is given by

$$\mathbf{F} = (F_\phi, F_z) = \rho_0 a \cos\phi \left[[u_z] \frac{[v'\theta']}{[\theta_z]} - [u'v'], \left(f - \frac{([u]\cos\phi)_\phi}{a\cos\phi} \right) \frac{[v'\theta']}{[\theta_z]} - [w'u'] \right], \tag{3}$$

where θ is potential temperature, f the Coriolis parameter, ρ_0 the surface density, w the vertical wind, and subscripts represent partial derivatives.

Under the quasigeostrophic approximation the EP flux is given by

$$\mathbf{F} = (F_\phi, F_z) = \rho_0 a \cos\phi \left(-[u'v'], f \frac{[v'\theta']}{[\theta_z]} \right), \tag{4}$$

which shows the dominant terms under such conditions. Latitudinal wave propagation is in the opposite sense to the horizontal eddy momentum flux and upward propagation is related to the poleward eddy heat flux. Figures presented in this section show the generalized EP flux computed using Eq. (3).

Figure 11 shows sector average composites of the low-frequency zonal wind and EP flux anomalies. The close
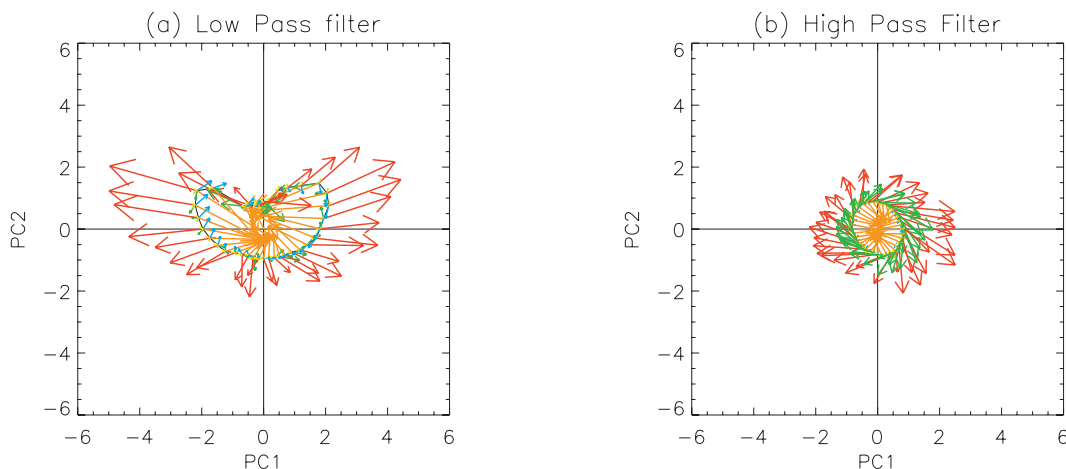
FIG. 10. Sector composite average trajectory (black line) using 32 phase space sectors for 30-day Lanczos (a) low-pass and (b) high-pass filtered data. Arrows show the projection of the vertically integrated momentum budget terms in PC1/PC2 phase space. Forcing by the zonally asymmetric eddies (C_{EDDY}) is represented in red and that by the zonally averaged flow (C_{ZONAL}) in blue; the surface stress ($[\tau_{S\lambda}]$) is shown in orange and the resultant wind tendency in green. The axes are scaled by $1/p_0$ owing to vertical integration.

similarity between the wind anomalies and the EOF structures in Fig. 1 is notable, including the poleward tilt with height on the equatorward side of the climatological jet. This confirms the dominant role of the leading two EOFs in the low-frequency variability. To a first approximation, anomalous upward EP flux (increased poleward eddy heat flux) is collocated with positive zonal wind anomalies at low frequencies, and vice versa. This is consistent with the EOF structures in Fig. 1, since the positive zonal wind anomalies are regions of increased temperature gradients (by thermal wind balance) and, so, areas of increased baroclinicity. The upward EP flux anomalies are associated with increased baroclinic wave amplitudes resulting from increased baroclinic growth. This collocation is consistent with the storm-track eddies and EP flux source migrating with the jet at low frequencies. Anomalous low-level EP flux divergence, also approximately collocated with the existing zonal wind anomaly pattern, acts as a westerly forcing to maintain the anomalous low-level flow against low-level drag. Similarly, the downward EP flux anomalies are collocated with easterly zonal wind anomalies. This is seen as the dominant radial balance in the vertically integrated momentum budget (Fig. 10a). It is a subtle mismatch in the latitude of the maximum EP flux divergence and wind anomalies that contribute to the phase space circulation at low frequencies. This will be investigated further in future work. The wind anomalies are more barotropic at higher latitudes in Fig. 11, suggesting a weakening of this wave–mean flow interaction on the poleward side of the jet.

At high frequencies (Fig. 12) the situation appears more complex. The sector-average composite wind anomalies have little vertical tilt, suggesting a modest but significant contribution of higher order EOFs to their structure. Close alignment between the low-level wind anomalies and their vertical integral leads to the more radial surface stress vectors seen in the high-frequency vertically integrated momentum budget in Fig. 10b. The EP flux anomalies are no longer collocated with the zonal wind anomalies, consistent with the flow evolving rapidly on short time scales. In fact, the strongest upward EP flux is closer to the latitude of the easterly wind anomaly, and vice versa. Despite this phase difference, the upward EP flux anomalies do appear to result from baroclinic growth in regions of increased baroclinicity. Recall that the high-frequency phase space circulation time scale is ~8 days. From the vertically integrated zonal momentum budget (Fig. 9), both the wind and EP flux anomalies grow on the poleward side of the midlatitude jet and move equatorward until they decay. In Fig. 12 a westerly wind anomaly appears near 70°N in sector $-+$ and migrates equatorward, following the panels clockwise, and decays in the subtropics in sector $++$ after just over one cycle. It is located near 50°N in sector $+-$ and upward EP flux occurs there in sector -0, ~3 days later. This apparent lagged response of the vertical EP flux to the baroclinicity (and hence wind anomalies) will be discussed further in reference to lagged correlations presented in Fig. 13.

The patterns of high-frequency EP flux in Fig. 12 appear consistent with the dependence of wave breaking
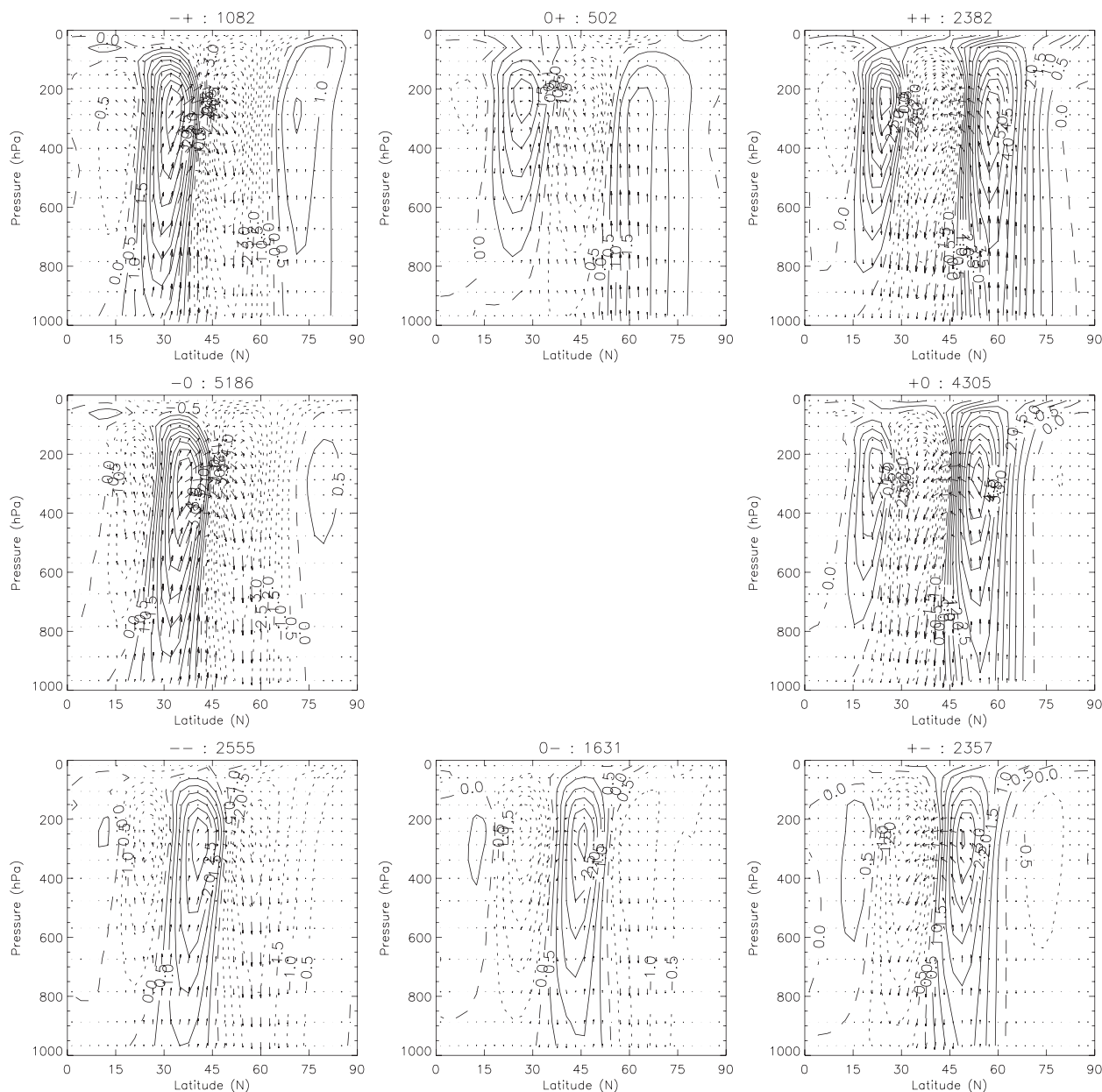
FIG. 11. Thirty-day Lanczos low-pass filter sector composites of zonal-mean zonal wind anomalies (contours) and EP flux anomalies (arrows) scaled as in Edmon et al. (1980). The title of each plot indicates the signs of PC1 and PC2 and the number of points in each composite picture. Contour interval is 0.5 m s^{-1} and dotted contours represent negative values.

on lateral shear, using the baroclinic life cycle paradigms of Thorncroft et al. (1993)[3] and studies such as those of Balasubramanian and Garner (1997) and Hartmann

_____

[3] The eddies are not explicitly filtered in our analysis. Instead, the high- and low-frequency covariances are composites based on the spectrum of the zonal wind, so it remains to be verified that the waves involved in the wave-breaking discussed here are dominated by high-frequency transients.

(2000). For sectors with upward anomalous EP flux poleward of ~45°N (e.g., sector −0), the anomalous horizontal flux is poleward, consistent with stronger cyclonic wave breaking (the LC2 baroclinic life cycle paradigm) on the poleward flank of the climatological jet and weaker anticyclonic wave breaking (the LC1 paradigm) on the equatorward flank. Similarly, for sectors with upward anomalous EP flux equatorward of ~45°N (e.g., sector +0), the opposite occurs, consistent with weaker

FIG. 12. As in Fig. 11 but using 30-day Lanczos high-pass filtered data.

LC2 behavior farther poleward and stronger LC1 behavior farther equatorward. Baroclinic life cycle experiments would need to be performed on each sector's mean state to verify this interpretation.

Comparing the low- and high-frequency sector composites of EP flux in Figs. 11 and 12, it is evident that the horizontal EP flux is in the same sense relative to the wind anomalies for both frequency bands (e.g., poleward for sector −0 and equatorward for +0). In contrast, the vertical EP flux, and, thus, the anomalous baroclinic wave source/sink, is in quite different locations. In the vertical

integral [and quasigeostrophic approximation, Eq. (4)] only the horizontal momentum flux contributes to eddy forcing of the integrated zonal mean flow, and it was evident from section 3d and Fig. 10 that the eddy forcing of low- and high-frequency variations is significantly different. The EP flux diagnostics suggest that it is phase differences, or equivalently displacements in latitude, between the vertically integrated EP flux divergence and wind anomalies that lead to the different forcing and behavior: slow poleward migration with superimposed rapid equatorward migration of anomalies.
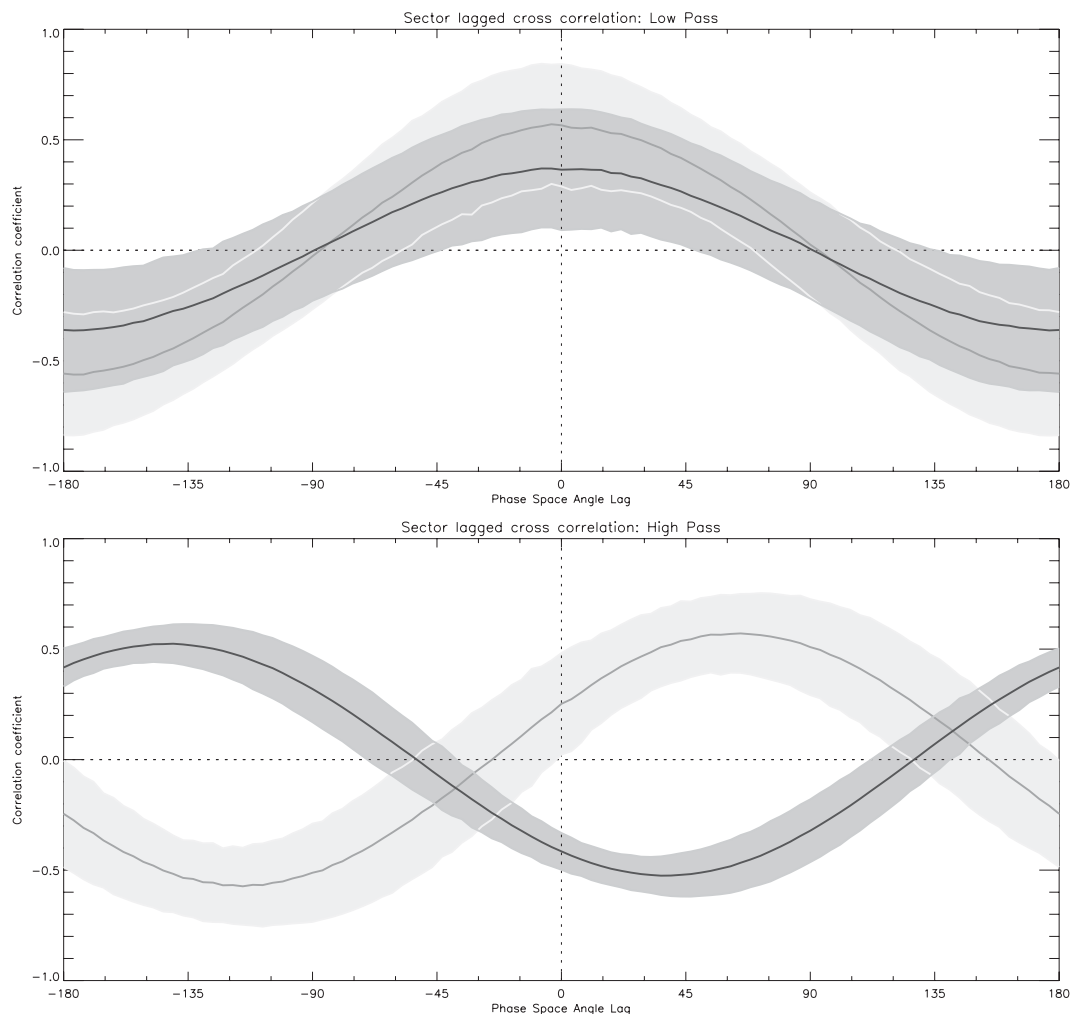
FIG. 13. Phase space angle lagged correlation of the zonal-mean zonal wind anomalies relative to the horizontal eddy momentum forcing (light gray) and the vertical component of the EP flux (dark gray), using 30-day Lanczos (top) low-pass and (bottom) high-pass filtered data. The lines show the mean correlation for a given lag over all of phase space and the shading shows ±1 standard deviation.

The phase space lag between the wind anomalies and F_z, and that between the wind anomalies and $\partial F_\phi/\partial y$, is now examined more closely at high and low frequencies. Note that $\partial F_\phi/\partial y$ corresponds to the first term on the rhs of Eq. (1) and has previously been referred to as eddy momentum forcing. Figure 13 shows correlations as a function of phase space angle lag between latitude–height sections of the wind anomalies and the vertical EP flux (in dark gray) and the horizontal eddy momentum forcing (in light gray). Note that at all frequencies the wind anomalies are in phase with the baroclinicity (as determined by the maximum Eady growth rate; not shown). At low frequencies both horizontal and vertical eddy terms are in phase with the winds, reflecting the quasi-equilibrium situation dominated by positive eddy feedback. At high frequencies the flow is strongly evolv-

ing and F_z (dark gray line) lags the zonal wind anomalies by 144° which, for a circulation time of ~8 days, translates to ~3 days. The horizontal eddy momentum forcing (light gray line) leads the wind anomalies by ~61° (or ~1 day). Similarly, the horizontal eddy momentum forcing lags F_z by ~4 days (not shown). Since circulations of phase space on short time scales are being considered, the phase lags contain an inherent ambiguity over assigning which term is truly leading or lagging. This is resolved in two ways. First, the poleward eddy heat flux (and hence F_z) occurs during the growth phase of baroclinic life cycles whereas the horizontal eddy momentum fluxes occurs in the decay phase, so the horizontal eddy momentum forcing is expected to lag F_z. Second, the vertically integrated momentum budget (Fig. 10b) shows the simultaneous phase angle of the various budget terms

for each sector of EOF phase space. There the wind tendency is approximately parallel to the horizontal eddy momentum forcing, and both lead the phase of the wind anomaly by 45° (or ~1 day). The resulting forcing/feedback loop of eddy–mean flow interaction sums to give the high-frequency τ_c of ~8 days.

4. Discussion and conclusions

The roles of EOF1 and EOF2 in the high- and low-frequency evolution can be examined by reconstructing the wind field from each EOF alone and from both together. Figure 14 shows low-frequency latitude phase angle sections of total and anomaly zonal-mean zonal wind field reconstructed using EOF1, EOF2, EOF1 plus EOF2, and the sum of all EOFs. As expected, EOF1 alone can capture the poleward migration of the mean jet and EOF2 alone captures the changes in the jet strength and width. However, EOF1 alone cannot change the jet strength at the jet center (45°). To capture the poleward migration of the jet with a constant strength and shape both EOF1 and EOF2 are required. Since EOF1 modifies lower climatological wind values on the flanks of the jet and EOF2 modifies the maximum climatological wind at the jet center, EOF2 requires smaller amplitudes to obtain the same jet strength as EOF1. In general, a single mode in quadrature with an extremum in the average state gives propagation of the total field but not of the anomaly, while a mode in phase with the extremum cannot give propagation in either. A combination of both modes is required for propagation of both total field and anomaly. So, only by combining EOF1 and EOF2 are poleward propagating zonal wind *anomalies* obtained. EOF2 is also important in capturing the subtropical variation and consequently in obtaining three propagating anomalies that reflect the overlap between the growth of new subtropical anomalies and the decay of polar anomalies. For both total and anomaly zonal wind fields the combined effect of EOF1 and EOF2 captures well the evolution found for the sum of all EOFs, although EOF1 provides a reasonable first approximation for the total wind field.

In many previous studies (e.g., Esler and Haynes 1999; LH2001; Lorenz and Hartmann 2003; Ring and Plumb 2007), the annular variability represented by each of the two leading modes, EOF1 and EOF2, has been considered separately. In view of the fact that the combined effect of EOF1 and EOF2 captures well the sum of all EOFs in both total and anomaly fields, important features of the flow are more readily apparent when considering a two-dimensional phase view.

Analysis of lagged cross-correlation data separately for each of the two modes of variability, such as presented by

LH2001, suggests eddy feedback is found only in EOF1 and not EOF2. Using a phase space view as presented here suggests that lagged cross-correlations between EOF1 and EOF2 may be important. These mixed mode cross-correlations (not shown) require careful interpretation, but do show signs that the projection of the eddy momentum forcing onto one EOF leads changes to the mean flow of the other EOF. From a phase space perspective, the sector lagged correlations between the eddy forcing and the wind that have been presented show the average picture over all phase angles. The eddy forcing and feedback can be seen clearly for the high-frequency flow, but at low frequencies the eddies and the winds are approximately in phase, reflecting the quasi-equilibrium situation.

In this paper a study of annular variability at high and low frequencies has been performed in a simplified atmospheric GCM. The first two leading modes of variability are used to characterize the latitudinal migration of the tropospheric jet in a two-dimensional phase space. In this phase space, EOF1 (x axis) corresponds to latitudinal jet shifts and EOF2 (y axis) to jet amplitudes and widths. Together EOF1 and EOF2 can describe the latitudinal migration of a jet of constant amplitude and width. Composites of the vertically integrated momentum equation for various regions of phase space are used to examine the forcing terms of the jet migration.

The high-frequency (less than 30 day) evolution is circular in phase space, which implies equal amplitude contributions from EOF1 and EOF2. Phase space trajectories and sector composites show equatorward propagation of the jet with a circulation time scale of ~8 days. The vertically integrated momentum budget shows strong eddy forcing of the flow in sector composites and phase space projections. EP flux composites similarly show large imbalances, in the form of phase differences and lags, between eddies and zonal wind anomalies. The vertical EP flux is a lagged response to the baroclinicity, and hence wind anomalies, of the rapidly evolving flow. EP flux composites suggest that the feedback of the eddies on the mean flow is consistent with traditional ideas of baroclinic life cycles.

The low-frequency (>30 day) evolution is elongated in phase space, indicating dominance by EOF1, but the curved shape of the distribution suggests a nonnegligible contribution from EOF2. Phase space sector composites of zonal-mean zonal wind show a poleward propagation of the jet followed by a collapse to a weak jet before the cycle begins again. Low-frequency variability in the idealized model here displays a broad spectrum of time scales, with an average "circulation time" in the EOF phase space of approximately 82 days. It is not clear how representative this is of real-world annular variability, and, indeed, there is discussion of unrealistically long time
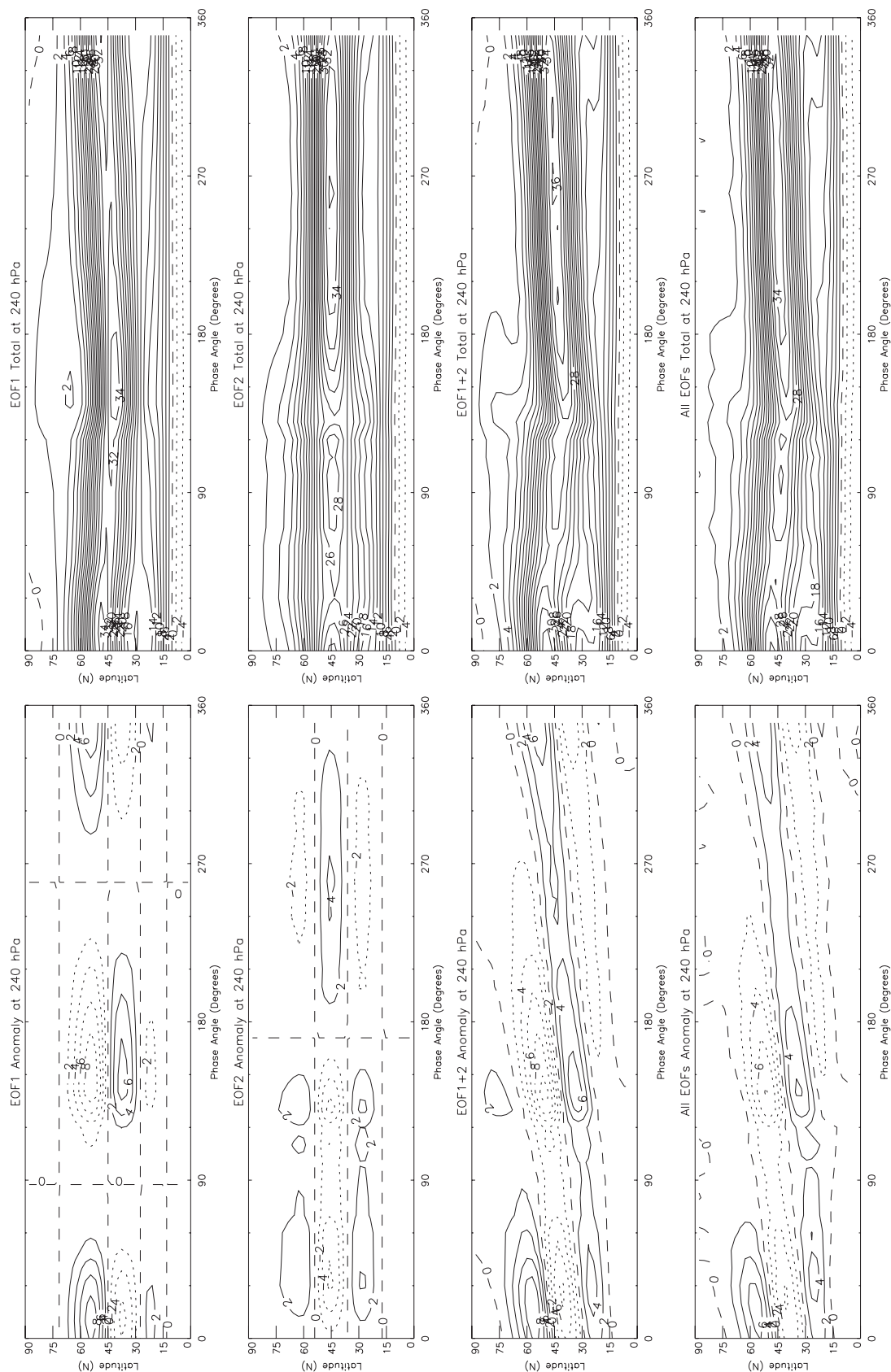
FIG. 14. Latitude phase angle sections of the (left) low-frequency 240-hPa wind anomalies and (right) total wind fields as constructed from (top row) EOF1, (second row) EOF2, (third row) EOF1 + EOF2, and (bottom row) all EOF components. Contour interval is 2 m s^{-1} and dotted contours represent negative values.
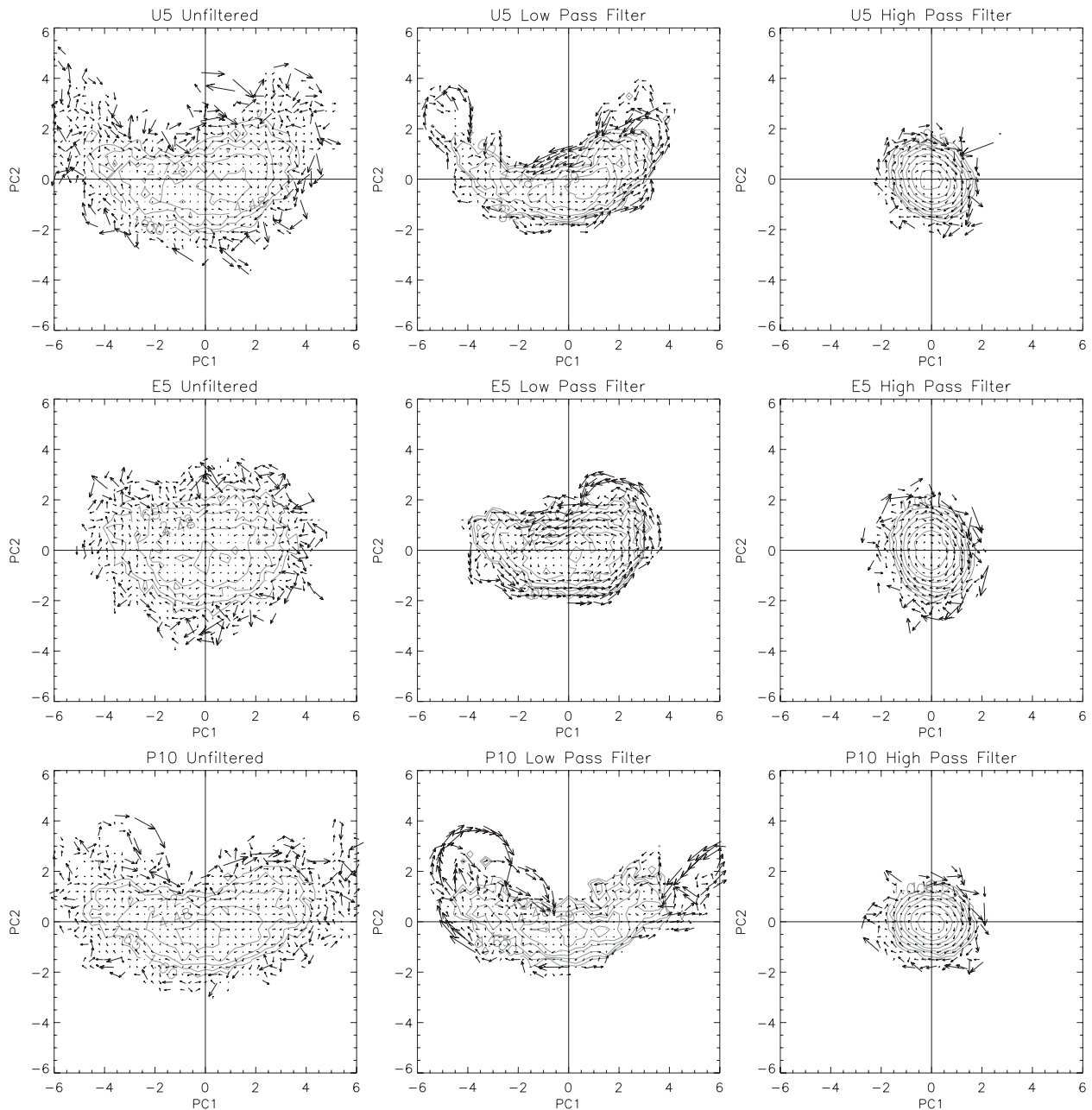
FIG. A1. As in Fig. 4 but for (top) run U5, (middle) run E5, and (bottom) run P10.

scales in similar idealized configurations (e.g., Gerber et al. 2008), possibly leading to unrealistically strong responses to stationary forcing. James and James (1992) found that low-frequency annular variability persisted in the presence of an imposed annual cycle in an idealized model similar to that used here. In reality, seasonal changes associated with land–sea contrast, including the tropical monsoons, might be expected to more strongly disrupt such annular variability, via their modulation of planetary wave forcing. There is evidence in idealized

models that the time scales of annular variability and the amplitude of the response to stationary forcing are modified by the presence of orography and longitudinal planetary-scale variations in baroclinicity (Gerber and Vallis 2007).

The vertically integrated momentum budget composites for low frequencies shows a close balance between the eddy forcing and surface friction. The evolution of the jet is the result of a small residual in this budget; however, it is the eddy forcing term that forces the flow. This

"quasi-equilibrium" interpretation is further supported by the EP flux sector composites and lagged correlations. Using a single cutoff time scale to define the low frequencies makes it difficult to determine a mechanism for the slow poleward propagation of the jet since the inclusion of the very low frequencies biases the results toward equilibrium. This problem will be addressed in Part II of this study, where the mechanisms involved are elucidated partly by use of more sophisticated temporal filtering.

APPENDIX

Simulations with Altered Temperature Distributions

Figure A1 shows phase space trajectories and density distributions equivalent to Fig. 4 for model simulations with altered stratospheric temperature distributions (as in HBD2005). The top row is taken from a run in which the stratospheric reference temperature is increased uniformly by 5 K (hereafter U5). The middle row corresponds to a simulation in which the stratospheric temperature is increased by 5 K at the equator decreasing with $\cos^2\phi$ to 0 K at the poles (hereafter E5). The bottom row corresponds to a simulation in which the stratospheric polar temperature is increased by 10 K, decreasing with latitude to 0 K at the equator (hereafter P10). For more details of the experimental design, see HBD2005. The left, middle, and right panels show the unfiltered, 30-day low-pass, and 30-day high-pass distributions, respectively, for each simulation.

The U5 and E5 simulations show anticlockwise (clockwise) trajectories at low (high) frequencies, similar to those of the control simulation presented in Fig. 4. As in the control, when the data are unfiltered there is no coherent phase space movement. For P10 the unfiltered and high-frequency behavior is again similar to the other simulations. However, at low frequencies there is little evidence of a coherent anticlockwise circulation of phase space. This is due to long periods in which the anomaly zonal wind field persists rather than propagates poleward but, as can be deduced from the top row of Fig. 14, this may still correspond to latitudinal migration of the jet in the total zonal wind field. Such persistent periods also occur in the control simulation, an example being days 1300–1400 of Fig. 5, but this behavior becomes more prevalent in P10. It is associated with a more elongated low-frequency density distribution, reflecting the more

dominant role of EOF1. The lack of coherent phase evolution arises because poleward and equatorward migrations of the jet (trajectories to the right and left, respectively, in the figures) are not statistically separated in their EOF2 amplitude. This behavior will be investigated in a further study and may be relevant for the zonal index regime noted by Son and Lee (2006) and Chan and Plumb (2009).

REFERENCES

Andrews, D. G., J. R. Holton, and C. B. Leovy, 1987: *Middle Atmosphere Dynamics.* Academic Press, 489 pp.
Balasubramanian, G., and S. T. Garner, 1997: The role of momentum fluxes in shaping the life cycle of a baroclinic wave. *J. Atmos. Sci.,* **54,** 510–533.
Baldwin, M. P., and T. J. Dunkerton, 1999: Downward propagation of the Arctic Oscillation from the stratosphere to the troposphere. *J. Geophys. Res.,* **104,** 30 937–30 946.
——, and ——, 2001: Stratospheric harbingers of anomalous weather regimes. *Science,* **294,** 581–584.
——, D. B. Stephenson, and I. T. Jolliffe, 2009: Spatial weighting and iterative projection methods for EOFs. *J. Climate,* **22,** 234–243.
Bates, J. R., 1981: A dynamical mechanism through which variations in solar ultraviolet radiation can influence tropopheric climate. *Sol. Phys.,* **74,** 399–415.
Chan, C. J., and A. R. Plumb, 2009: The response to stratospheric forcing and its dependence on the state of the troposphere. *J. Atmos. Sci.,* **66,** 2107–2115.
——, ——, and I. Cerovecki, 2007: Annular modes in a multiple migrating zonal jet regime. *J. Atmos. Sci.,* **64,** 4053–4068.
Charlton, A. J., A. O. O'Neill, W. A. Lahoz, and A. Massacand, 2004: Sensitivity of tropospheric forecasts to stratospheric initial conditions. *Quart. J. Roy. Meteor. Soc.,* **130,** 1771–1792.
Crooks, S. A., and L. J. Gray, 2005: Characterization of the 11-year solar signal using a multiple regression analysis for the ERA-40 dataset. *J. Climate,* **18,** 996–1015.
Edmon, H. J., B. J. Hoskins, and M. E. McIntyre, 1980: Eliassen–Palm cross sections for the troposphere. *J. Atmos. Sci.,* **37,** 2600–2616.
Esler, J. G., and P. H. Haynes, 1999: Baroclinic wave breaking and the internal variability of the tropospheric circulation. *J. Atmos. Sci.,* **56,** 4014–4031.
Gerber, E. P., and G. K. Vallis, 2007: Eddy–zonal flow interactions and the persistence of the zonal index. *J. Atmos. Sci.,* **64,** 3296–3311.
——, S. Voronin, and L. M. Polvani, 2008: Testing the annular mode autocorrelation time scale in simple atmospheric general circulation models. *Mon. Wea. Rev.,* **136,** 1523–1536.
Haigh, J. D., 1994: The role of stratospheric ozone in modulating the solar radiative forcing of climate. *Nature,* **370,** 544–546.
——, 1996: The impact of solar variability on climate. *Science,* **272,** 981–984.
——, 2003: The effects of solar variability on the earth's climate. *Philos. Trans. Roy. Soc. London,* **A361,** 95–111.
——, M. Blackburn, and R. Day, 2005: The response of tropospheric circulation to perturbations in lower stratospheric temperature. *J. Climate,* **18,** 3672–3685.
Hartmann, D. L., 2000: The key role of lower-level meridional shear in baroclinic wave life cycles. *J. Atmos. Sci.,* **57,** 389–401.

Haynes, P. H., 2005: Stratosphere–troposphere dynamical coupling. *SPARC Newsletter,* No. 25, SPARC International Project Office, Toronto, ON, Canada, 27–31.

Held, I. M., and M. J. Suarez, 1994: A proposal for the intercomparison of the dynamical cores of atmospheric general circulation models. *Bull. Amer. Meteor. Soc.,* **75,** 1825–1830.

Hoskins, B. J., and A. J. Simmons, 1975: A multi-layer spectral model and the semi-implicit method. *Quart. J. Roy. Meteor. Soc.,* **101,** 637–655.

James, I. N., and P. M. James, 1992: Spatial structure of ultra-low-frequency variability of the flow in a simple atmospheric circulation model. *Quart. J. Roy. Meteor. Soc.,* **118,** 1211–1233.

——, and J. P. Dodd, 1996: A mechanism for the low-frequency variability of the mid-latitude troposphere. *Quart. J. Roy. Meteor. Soc.,* **122,** 1197–1210.

James, P. M., K. Fraedrich, and I. N. James, 1994: Wave-zonal-flow interaction and ultra-low-frequency variability in a simplified global circulation model. *Quart. J. Roy. Meteor. Soc.,* **120,** 1045–1067.

Kodera, K., 2006: Influence of stratospheric sudden warming on the equatorial troposphere. *Geophys. Res. Lett.,* **33,** L06804, doi:10.1029/2005GL024510.

——, and K. Shibata, 2006: Solar influence on the tropical stratosphere and troposphere in the northern summer. *Geophys. Res. Lett.,* **33,** L19704, doi:10.1029/2006GL026659.

Kuroda, Y., and K. Kodera, 2005: Solar cycle modulation of the southern annular mode. *Geophys. Res. Lett.,* **32,** L13802, doi:10.1029/2005GL022516.

——, M. Deushi, and K. Shibata, 2007: Role of solar activity in the troposphere–stratosphere coupling in the Southern Hemisphere winter. *Geophys. Res. Lett.,* **34,** L21704, doi:10.1029/2007GL030983.

Kushner, P. J., and L. M. Polvani, 2004: Stratospheric–tropospheric coupling in a relatively simple AGCM: The role of eddies. *J. Climate,* **17,** 629–639.

Lee, S., S. W. Son, K. Grise, and S. B. Feldstein, 2007: A mechanism for the poleward propagation of zonal mean flow anomalies. *J. Atmos. Sci.,* **64,** 849–868.

Lorenz, D. J., and D. L. Hartmann, 2001: Eddy–zonal flow feedback in the Southern Hemisphere. *J. Atmos. Sci.,* **58,** 3312–3327.

——, and ——, 2003: Eddy–zonal flow feedback in the Northern Hemisphere winter. *J. Climate,* **16,** 1212–1227.

——, and E. T. DeWeaver, 2007: Tropopause height and zonal wind response to global warming in the IPCC scenario integrations. *J. Geophys. Res.,* **112,** D10119, doi:10.1029/2006JD008087.

Ring, M. J., and A. R. Plumb, 2007: Forced annular mode patterns in a simple atmospheric general circulation model. *J. Atmos. Sci.,* **64,** 3611–3626.

Salby, M. L., and P. F. Callaghan, 2006: Evidence of the solar cycle in the tropical troposphere. *J. Geophys. Res.,* **111,** D21113, doi:10.1029/2006JD007133.

Simmons, A. J., and D. M. Burridge, 1981: An energy and angular-momentum conserving vertical finite-difference scheme and hybrid vertical coordinates. *Mon. Wea. Rev.,* **109,** 758–766.

Simpson, I., M. Blackburn, and J. D. Haigh, 2009: The role of eddies in driving the tropospheric response to stratospheric heating perturbations. *J. Atmos. Sci.,* **66,** 1347–1365.

Son, S.-W., and S. Lee, 2006: Preferred modes of variability and their relationship with climate change. *J. Climate,* **19,** 2063–2075.

Song, Y., and W. A. Robinson, 2004: Dynamical mechanisms for stratospheric influence on the troposphere. *J. Atmos. Sci.,* **61,** 1711–1725.

Thorncroft, C. D., B. J. Hoskins, and M. E. McIntyre, 1993: Two paradigms of baroclinic-wave life-cycle behaviour. *Quart. J. Roy. Meteor. Soc.,* **119,** 17–55.

Vallis, G. K., and E. P. Gerber, 2007: Local and hemispheric dynamics of the North Atlantic Oscillation, annual patterns and the zonal index. *Dyn. Atmos. Oceans,* **44,** 184–212.

Wittman, M. A. H., L. M. Polvani, R. K. Scott, and A. J. Charlton, 2004: Stratospheric influence on baroclinic lifecycles and its connection to the Arctic Oscillation. *Geophys. Res. Lett.,* **31,** L16113, doi:10.1029/2004GL020503.

Yin, J. H., 2005: A consistent poleward shift of the storm tracks in simulations of 21st century climate. *Geophys. Res. Lett.,* **32,** L18701, doi:10.1029/2005GL023684.